Nanoscale

PAPER

Check for updates

Electronic redistribution through the interface of $MnCo_2O_4$–Ni_3N nano-urchins prompts rapid *In situ* phase transformation for enhanced oxygen evolution reaction†

Ashish Gaur,‡ Aashi,‡ Joel Mathew John, Vikas Pundir, Rajdeep Kaur, Jatin Sharma, Kaustubhi Gupta, Chandan Bera (ID) and Vivek Bagchi (ID) *

One of the most coveted objectives in the realm of energy conversion technologies is the development of highly efficient and economically viable electrocatalysts for the oxygen evolution reaction. The commercialization of such techniques has thus far been impeded by their slow response kinetics. One of the many ways to develop highly effective electrocatalysts is to judiciously choose a coupling interface that maximizes catalyst performance. In this study, the *in situ* electrochemical phase transformation of $MnCo_2O_4$–Ni_3N into $MnCo_2O_4$–NiOOH is described. The catalyst has an exceptional overpotential of 224 mV to drive a current density of 10 mA cm^{-2}. Strong interfacial contact is seen in the $MnCo_2O_4$–Ni_3N catalyst, leading to a considerable electronic redistribution between the $MnCo_2O_4$ and Ni_3N phases. This causes an increase in the valence state of Ni, which makes it an active site for the adsorption of *OH, O*, and *OOH (intermediates). This charge transfer facilitates the rapid phase transformation to form NiOOH from Ni_3N. At a higher current density of 300 mA cm^{-2}, the catalyst remained stable for a period of 140 h. DFT studies also revealed that the *in situ*-formed NiOOH on the $MnCo_2O_4$ surface results in superior OER kinetics compared to that of NiOOH alone.

Introduction

We have never been more susceptible to the potentially disastrous repercussions of climate change than we are right now. A dramatic change in both the temperature and the pattern of the weather has resulted as a direct consequence of severe human activities such as warfare, vast space exposition, and numerous other steps that emit greenhouse gases. This has resulted in significant dangers to all forms of life on the planet.[1] Hence, it is vital to solve the ever-increasing petrochemical energy crises and environmental pollution concerns by creating sustainable and green energy sources.[2–5] For oxygen/hydrogen production, electrocatalytic water splitting has attracted great attention. However, the sluggishness of the reaction kinetics of the oxygen evolution reaction (OER) and its complex reaction mechanism are barriers to the water splitting reaction.[6–8] In general, the OER entails a multi-step four-electron transfer.[9–12] It is still difficult to speed up the electron

transfer process in the OER at the same time by merely changing the charge of the electrocatalyst.[13,14] Recently, first-row transition metal-based spinel oxides have been widely investigated as potential materials for OER due to their excellent durability under elevated anodic potential and the interaction of their inner multivalent states.[15,16] The existence of tetrahedral and octahedral sites in the spinel structure offers numerous locations for accommodating various transition-metal cations in a variety of valence states to generate a substantial number of oxides.[17–20] In all the spinel oxides, the intrinsic conductivity is very low due to their semiconducting nature and the small number of active sites.[21,22] Recent theoretical and experimental investigations have already shown that Ni_3N is a very intriguing material in this scenario, since it has certain surface terminations and crystal facets that can provide optimal energetics for water dissociation.[23–25] Different fabrications of metal-nitride-based electrocatalysts have been developed to further increase the effectiveness of the water splitting performance of metal nitrides such as Ni_3N–NiMoN/CC, Ru/Ni_3N–Ni and Co–Ni_3N.[26–28] In all these materials, the Ni atoms have a low oxidation state, which makes them electron-rich with a filled e_g orbital. However, the activity of the Ni-based materials can be further enhanced by the enhanced valence state of the Ni atoms. Higher-valent Ni metal atoms can

Institute of Nano Science and Technology, Sector-81, Knowledge City, Sahibzada Ajit Singh Nagar, Punjab, Pin – 140306, India. E-mail: bagchiv@inst.ac.in

tremendously enhance the OER by enhancing the rate of adsorption of intermediates (OH*, O* and OOH*) on the active sites.[29–32] Interface coupling has a significant effect on electrocatalytic behaviour through electronic modulation of the surface atoms present at the interface, adjusting the overlap of orbitals between different atoms, and ultimately optimizing the attachment of the intermediates on the electrode surface.[33–37]

Meanwhile, the findings of theoretical simulations and experimental characterizations have shown that the *in situ* formed metal oxyhydroxides on the outermost layer of metal nitrides are active species that accelerate the OER kinetics.[38,39] As an illustration, Schuhmann and his coworkers demonstrated that the conversion of Co_2N into more active CoOOH can boost the OER kinetics.[40] Therefore, choosing the appropriate solid for Ni_3N to develop a composition in which the interfacial interaction can significantly enhance the phase transformation of the Ni_3N phase to construct the more-active NiOOH phase.

Herein, using the interfacial interaction technique, we formed novel heterointerfaces of $MnCo_2O_4$–Ni_3N over nickel foam (Scheme 1). The electrodeposition technique was used for the synthesis of $Ni(OH)_2$ nanosheets over $MnCo_2O_4$ nanowires. Further nitridation in the presence of ammonia produces the Ni_3N nanosheets over the $MnCo_2O_4$ nanowire scaffold. The heterostructure undergoes rapid phase transformation to generate more efficient NiOOH species. This heterostructure shows impressive OER activity, achieving an overpotential of 224 mV (@ 10 mA cm^{-2}). The durability of the catalyst is also excellent, with no change in current density (300 mA cm^{-2}) even after 140 h of stability testing. Charge transfer from Ni_3N to $MnCo_2O_4$ has been observed and characterized using X-ray photoelectron spectroscopy (XPS). The presence of high-valent Mn^{3+} and Co^{3+} in $MnCo_2O_4$ makes it of high polarity, which results in electronic uptake from the Ni_3N phase through the interface. This reallocation of electrons through the interface leads to the enhancement of the Ni valence state and enhances the adsorption of OH^- ions, which simultaneously increases the catalytic performance towards the oxygen evolution reaction (OER) by reconstructing the phase to form more active NiOOH species. We have also carried out DFT calculations of the $MnCo_2O_4$–NiOOH heterostructure, and the results showed that the NiOOH that is created over the surface of $MnCo_2O_4$ possesses a higher level of activity compared to NiOOH alone.

Experimental section

Materials

All chemicals are purchased from a variety of sources and utilised in their original forms. Manganese(II) chloride tetrahydrate ($MnCl_2\cdot4H_2O$, 99.9%), cobalt(II) nitrate hexahydrate (Co(NO_3)$_2\cdot6H_2O$, 98%), nickel(II) nitrate hexahydrate (Ni(NO_3)$_2\cdot6H_2O$, 98%), ammonium fluoride (NH_4F, 99.9%), urea (NH_2CONH_2, 99.5%), potassium hydroxide pellets (KOH) and ruthenium(IV) oxide (RuO_2, 99.9% trace metal basis) were purchased from Sigma Aldrich. Nanoshel was the supplier of nickel foam (NF). For every step of the preparation, Milli-Q water with a conductivity of 0.056 S cm^{-1} was used.

Synthesis of $MnCo_2O_4$ nanowires on NF

To cleanse the surface and remove any unwanted coatings, the NF was gently washed with DI water and acetone after being cleaned with a 3 M HCl solution that was ultrasonically agitated. The cleaned NF was divided into small pieces with a 1 cm × 1.5 cm cross-sectional area. The hydrothermal method was used to grow nanowires of $MnCo_2O_4$. A homogeneous solution of 0.280 g Co(NO_3)$_2\cdot6H_2O$, 0.088 g $MnCl_2\cdot4H_2O$, 0.068 g NH_4F, and 0.051 g urea was made using 5 mL of ethanol and 25 mL of DI water. The above-described solution was placed in a Teflon-lined stainless-steel autoclave, and one piece of NF was placed in the autoclave. The autoclave was heated at 120 °C for 12 h. The as-synthesized MnCoLDH/NF was removed from the autoclave and rinsed with ethanol and DI water. After washing, the electrode was dried at 60 °C over-
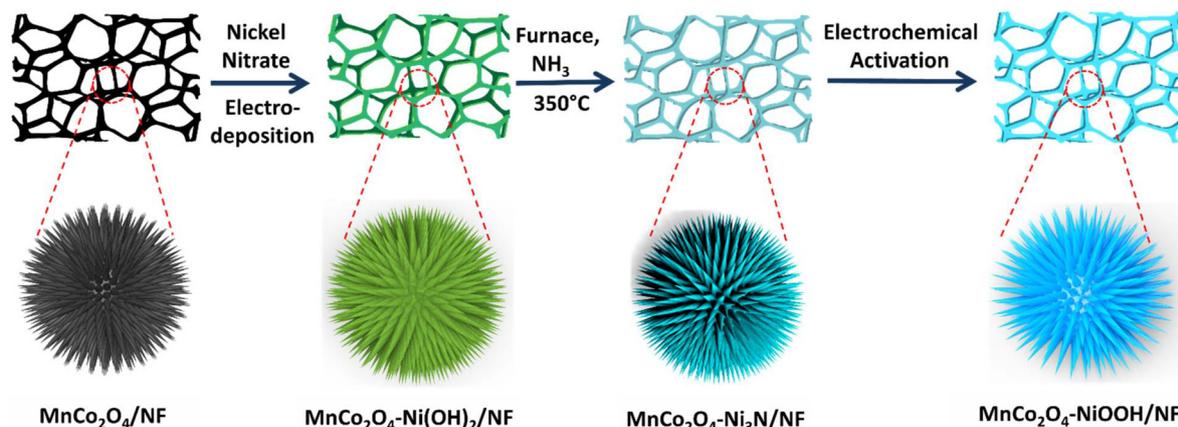
Scheme 1 Formation of $MnCo_2O_4$–NiOOH nano-urchins over nickel foam.

night. Finally, the as-prepared MnCoLDH/NF electrode was calcined in air for 2 hours at 350 °C to form $MnCo_2O_4$ over nickel foam.

Synthesis of $MnCo_2O_4$–Ni_3N

Nickel hydroxide nanosheets were electrodeposited over $MnCo_2O_4$/NF. The fabrication of $Ni(OH)_2$ was done using a three-electrode setup in which $MnCo_2O_4$/NF, Ag/AgCl, and graphite rod were used as the working, reference, and counter electrodes, respectively. The electrolyte was prepared using an aqueous solution of 0.2 M $Ni(NO_3)_2 \cdot 6H_2O$. The deposition potential was kept at −2.0 V for 600 seconds. Following this step, the deposition of $Ni(OH)_2$ onto the $MnCo_2O_4$/NF substrate occurred. This $MnCo_2O_4$–$Ni(OH)_2$ electrode was heated in a furnace at 350 °C under a constant NH_3 flow for 2 h. Ni$(OH)_2$ was transformed into Ni_3N sheets over the $MnCo_2O_4$ nanowire. The obtained $MnCo_2O_4$–Ni_3N catalyst was washed with DI and ethanol several times and used as a working electrode. The synthesis of $MnCo_2O_4$ and Ni_3N individually, along with the physical characterization and electrochemical analysis details, are provided in ESI S1.1 and 1.2.†

Synthesis of $MnCo_2O_4$–NiOOH

$MnCo_2O_4$–NiOOH was fabricated *in situ* through anodic oxidation of the $MnCo_2O_4$–Ni_3N. A three-electrode setup was used, in which a graphite rod was the counter electrode, Ag/AgCl was the reference electrode and $MnCo_2O_4$–Ni_3N was used as a working electrode. In addition, 1 M KOH was used as the electrolyte. The catalyst was formed by conducting 50 LSV cycles in the potential range of 0 to 1 V (*vs.* RHE). The scan rate was kept at 5 mV s^{-1}. The phase transformation of $MnCo_2O_4$–Ni_3N occurred to give $MnCo_2O_4$–NiOOH.

Results and discussion

As shown in Scheme 1, the catalyst $MnCo_2O_4$–Ni_3N was produced using the temperature-controlled nitridation of $MnCo_2O_4$–$Ni(OH)_2$ under the indicated conditions. Electron transport between Ni_3N and $MnCo_2O_4$ is facilitated by the presence of a heterointerface between the two materials. NiOOH is produced from Ni_3N upon electrochemical activation and can catalyse the oxygen evolution reaction (OER). Structural elucidation of all the catalysts was conducted using PXRD analysis. The PXRD pattern of $MnCo_2O_4$–Ni_3N is shown in Fig. 1a. This pattern confirms the formation of $MnCo_2O_4$ and Ni_3N with a set of obvious diffraction peaks corresponding to the cubic and hexagonal phases of $MnCo_2O_4$ (JCPDS No. 23-1237) and Ni_3N (JCPDS No. 70-9598), respectively.[41–43] The electronic structure, chemical states, and electronic redistribution in $MnCo_2O_4$–Ni_3N, $MnCo_2O_4$ and, Ni_3N were investigated using X-ray photoelectron spectroscopy analysis (XPS). The wide-scan XPS spectra of $MnCo_2O_4$–Ni_3N, MnCo2O4, and Ni_3N can be found in ESI S2.1 Fig. S1.† We observed three peaks in the Ni 2p spectrum of MnCo2O4–Ni_3N (Fig. 1b), with centres located at 853.2, 856.3, and 860.7 eV, respectively. These peaks are

attributed to the existence of Ni–N and Ni–O, in addition to one satellite peak of Ni 2p$_{3/2}$. Furthermore, the presence of all three peaks is also evident in the context of Ni2p$_{1/2}$ splitting at 870.5, 873.6, and 878.6 eV.[27,44] These peaks can also be seen in the Ni 2p XPS spectra of Ni_3N alone (Fig. 1b), but at a somewhat lower binding energy. The increased binding energy of Ni 2p in $MnCo_2O_4$–Ni_3N implies that charge is being transferred from Ni to another atom. The N 1s spectrum (Fig. 1c) for $MnCo_2O_4$–Ni_3N shows a peak at 398.7 eV, which is attributed to the metal–nitrogen bond.[45,46] The N 1s spectra of Ni_3N exhibits the peak for the M–N bond at a significantly lower binding energy.

The investigation was further extended to the Mn2p XPS spectra of $MnCo_2O_4$–Ni_3N and $MnCo_2O_4$. We observed four peaks in the Mn2p spectrum of the catalyst at 640.0, 641.3, 652.1, and 652.2 eV corresponding to the Mn^{2+} and Mn^{3+} peaks of Mn2p$_{3/2}$ and Mn2p$_{1/2}$ splitting (Fig. 1d). All four peaks are also detected in the Mn2p spectrum of $MnCo_2O_4$ alone, but at higher binding energy. Similarly, in the Co2p XPS spectrum of $MnCo_2O_4$–Ni_3N, we observed three peaks at 779.1, 781.6, and 785.7 eV for Co^{3+}, Co^{2+}, and one satellite peak of Co2p$_{3/2}$ splitting (Fig. 1e). The other three peaks at 795.0, 796.9 and 801.7 eV correspond to Co^{3+}, Co^{2+} and one satellite peak of Co2p$_{1/2}$ splitting.[47,48] Similarly, the Co2p spectra of pure $MnCo_2O_4$ show all six peaks, but with a higher binding energy. Even the O 1s spectrum showed this same pattern (Fig. 1f). The O 1s spectrum of $MnCo_2O_4$–Ni_3N shows three peaks labelled as O1, O2, and O3 at 528.8, 530.4, and 532.0 eV. The peaks O1 and O2 correspond to the presence of O^{2-}, which is indicative of the formation of spinel $MnCo_2O_4$.[49–51] The peak O3 corresponds to the presence of chemisorbed oxygen. These three peaks are consistent with the O 1s spectra of pure $MnCo_2O_4$, but are found at higher binding energies. The shift towards higher binding energies for Ni and N and the shift towards lower binding energy in the case of Mn, Co, and O confirms the charge transfer from Ni_3N to $MnCo_2O_4$. As a result of the valence-state enhancement of Ni caused by the transfer of charges, the Ni surfaces become excellent adsorption sites for O*, *OH and HOO* intermediate species. This rapid adsorption of intermediates is responsible for the rapid phase transformation of Ni_3N into NiOOH, which further enhances the reaction kinetics for the OER. The conversion of Ni_3N to NiOOH was further confirmed from the XPS spectra. The peak corresponding to the existence of Ni–N disappeared (Fig. 1g). The XPS spectra of Co2p (Fig. 1h) and Mn2p (Fig. 1i) remained the same, as there was no change in the $MnCo_2O_4$ phase. The XPS spectra of O 1s is provided in ESI S2.2 Fig. S2.†

To understand the morphology of the $MnCo_2O_4$–Ni_3N catalyst, FESEM analysis was carried out at each step. We observed the fine nanowires of $MnCo_2O_4$ collectively formed a nano-urchin-like morphology (Fig. 2a and b). Subsequently, fine nanosheets of Ni_3N were grown over the surface of the $MnCo_2O_4$ nanowires. The $MnCo_2O_4$–Ni_3N nano-urchins are depicted in Fig. 2c and d. During the OER, the Ni_3N phase was converted into NiOOH, and the surface of the nano-urchins also became rough due to the presence of more exposed
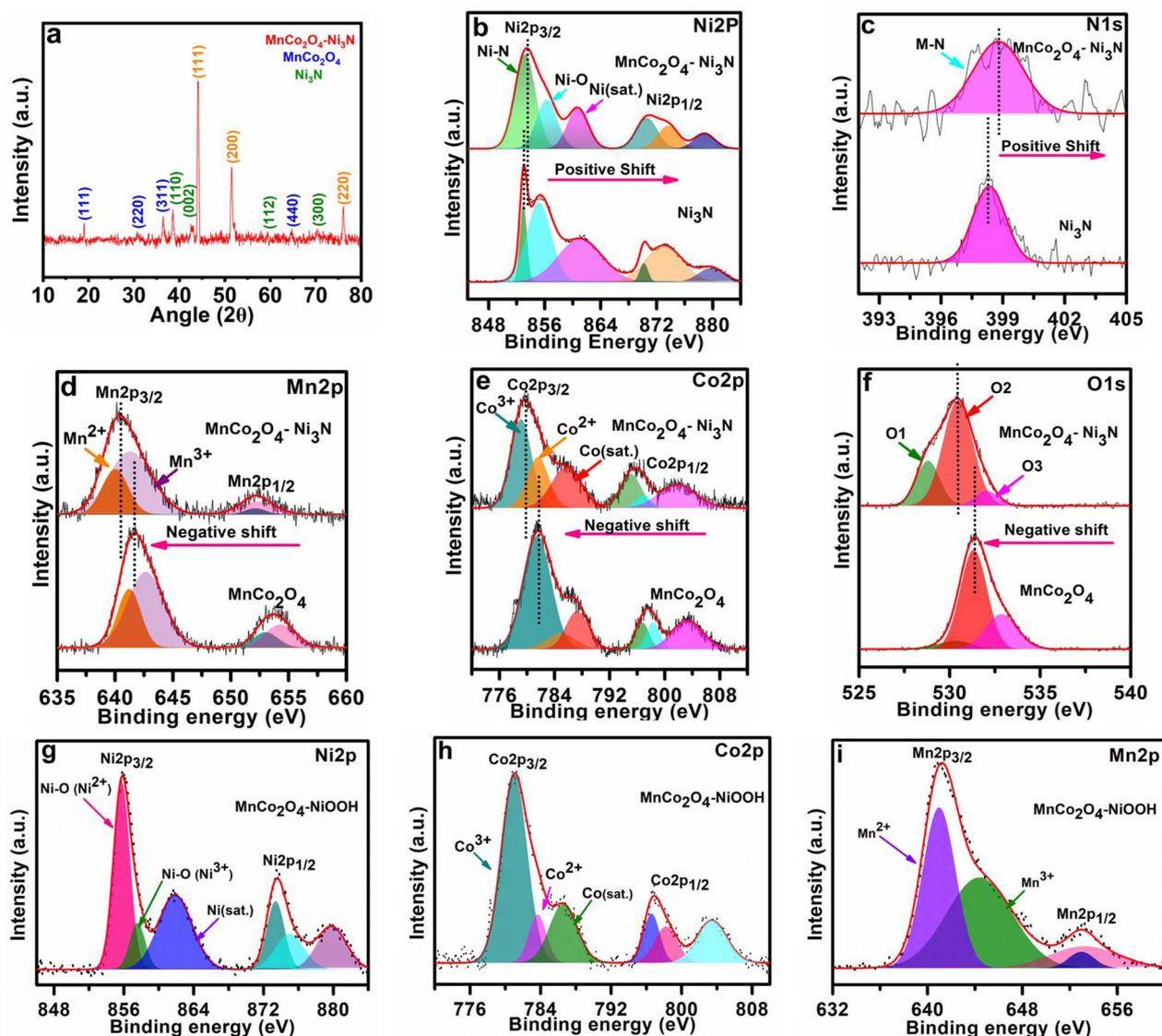
Fig. 1 (a) PXRD pattern of $MnCo_2O_4-Ni_3N$. High-resolution (b) Ni2p present in $MnCo_2O_4-Ni_3N$ and Ni_3N. (c) N1s present in $MnCo_2O_4-Ni_3N$ and Ni_3N. (d) Mn2p, (e) Co2p and (f) O1s present in $MnCo_2O_4-Ni_3N$ and $MnCo_2O_4$. (g) Ni2p (h) Co2p and (i) Mn2p XPS spectra of $MnCo_2O_4-NiOOH$.

NiOOH on the surface. The SEM images of $MnCo_2O_4-NiOOH$ are provided in Fig. 2e and f.

Examination with a transmission electron microscope (TEM) was also carried out to gain additional understanding regarding the shape and microstructure of the $MnCo_2O_4-$NiOOH catalysts. Fig. 3a shows the TEM image of a $MnCo_2O_4$ nanowire, whereas the presence of NiOOH nanosheets over the surface of $MnCo_2O_4$ nanowires can be seen in Fig. 3b and c. To confirm the presence of $MnCo_2O_4$ and NiOOH in the catalyst, HRTEM analysis was carried out. Fig. 3d–f show an HRTEM image of the catalyst with fringe widths of 0.25 and 0.22 nm corresponding to the (311) plane of $MnCo_2O_4$ and (102) plane of NiOOH.[41]

The phenomenon of superhydrophilicity, which is characterized by a the strong affinity of a surface for water, resulting

in a thin dispersion of water and the absence of droplet formation, can exert a substantial impact on the electrocatalytic processes. Efficient contact between the catalyst surface and the electrolyte is crucial for electrolysis and other electrochemical reactions. The impact of superhydrophilicity on electrocatalysis can explained by the enhanced surface wettability, increased mass transport and reduction in concentration polarization.[52–54] The contact angle of the surface of bare nickel foam was measured to be 116.7°, making it hydrophobic (ESI S3 Fig. S3.1†). On the other hand, the surface of $MnCo_2O_4-NiOOH$ was found to have a contact angle of 0°, making it superhydrophilic (Fig. 3g and h). We also analyzed the surface behaviour of the $MnCo_2O_4$ and NiOOH; the $MnCo_2O_4$ was found to be hydrophobic, whereas the surface of the NiOOH was found to be superhydrophilic (ESI S3.2
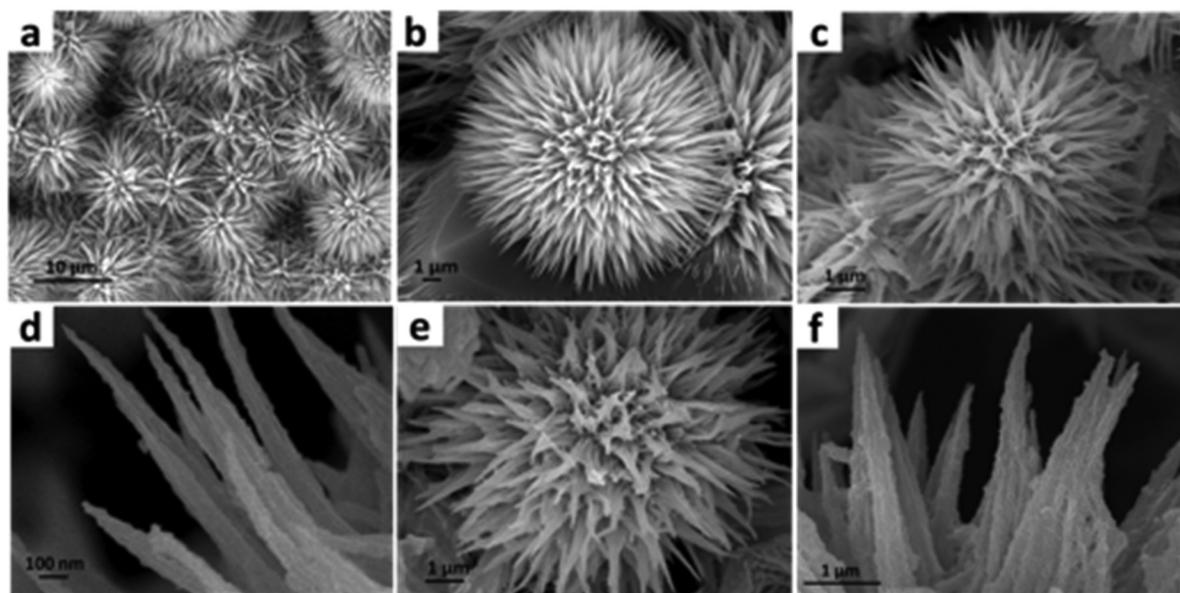
Fig. 2 (a) and (b) FESEM images of $MnCo_2O_4$ nano-urchins at different magnifications. (c) and (d) Ni_3N grown over $MnCo_2O_4$ nano-urchins. (e) and (f) NiOOH grown over $MnCo_2O_4$ nano-urchins.
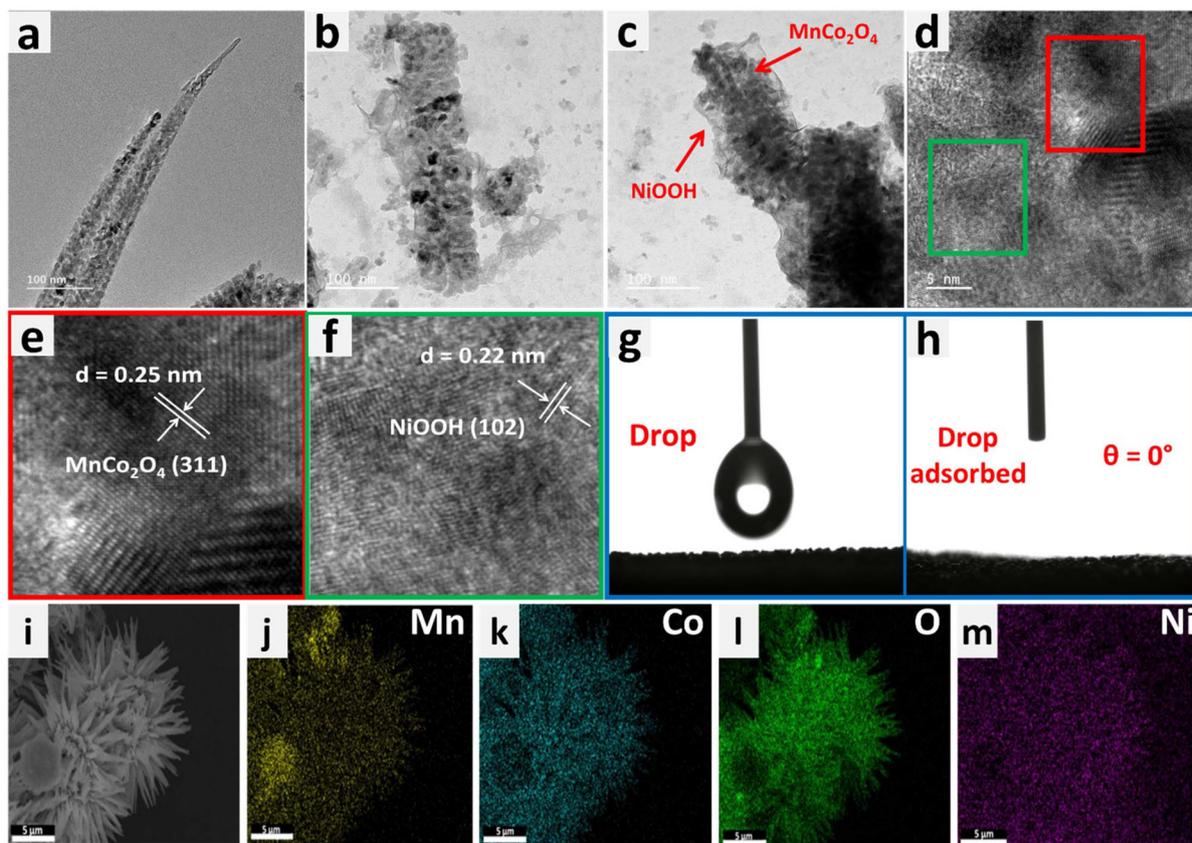
Fig. 3 (a) TEM images of a $MnCo_2O_4$ nanowire and (b) and (c) NiOOH nanosheets grown over a $MnCo_2O_4$ nanowire. (d) HRTEM image of $MnCo_2O_4$–NiOOH confirming the presence of (e) $MnCo_2O_4$ and (f) NiOOH. (g) and (h) Hydrophilicity analysis using drop shape analysis for $MnCo_2O_4$–NiOOH. (i) Image on which elemental mapping was carried out and the fine distributions of (j) Mn, (k) Co, (l) Ni and (m) O.

Fig. S4†). The even distribution of Mn, Co, Ni, and O over the catalyst scaffold was verified using FESEM elemental mapping (Fig. 3(i)–(m)).

Electrochemical

After the catalysts were developed, further studies were carried out in an aqueous electrolyte using a three-electrode setup to investigate the electrocatalytic capabilities of the catalysts in the oxygen evolution reaction (OER). The catalyst was generated *in situ* by conducting linear sweep voltammetry in the potential range of 1 to 2 V (*vs.* RHE). The $MnCo_2O_4$–Ni_3N electrode was transformed rapidly into the $MnCo_2O_4$–NiOOH electrode as soon as the OER process started. This rapid phase modification of $MnCo_2O_4$–Ni_3N into $MnCo_2O_4$–NiOOH is due to the strong interfacial contact within the $MnCo_2O_4$ and Ni_3N phase. We confirmed this by the position of the oxidation peak of Ni ($Ni^{2+} \rightarrow Ni^{3+}$). The position of the oxidation peak is at 1.40 V (*vs.* RHE) for the oxidation of the bare Ni_3N electrode,

whereas for the heterostructure $MnCo_2O_4$–Ni_3N it is at 1.33 V (*vs.* RHE) (Fig. 4a). This shows that the potential required for the oxidation of the Ni_3N present in $MnCo_2O_4$–Ni_3N is much lower than that of the pure Ni_3N phase. Fig. 4b shows the polarization curves of $MnCo_2O_4$–NiOOH, $MnCo_2O_4$, NiOOH and commercially available RuO_2.

At a current density of 10 mA cm^{-2}, an overpotential of 224, 270, 300, and 350 mV was obtained for $MnCo_2O_4$–NiOOH, RuO_2, $MnCo_2O_4$, and NiOOH, respectively. The $MnCo_2O_4$–NiOOH heterostructure outperforms RuO_2 as well as all the supporting catalysts at all current densities. Fig. 4c provides an insightful comparison of the overpotential at a current density of 10 mA cm^{-2} for all the catalysts. To gain a deeper comprehension of the kinetics of the catalysts, the value of the Tafel slope was determined by linear fitting of the polarization curve (Fig. 4d). A Tafel slope value of 111 mV dec^{-1} is obtained for the $MnCo_2O_4$–NiOOH heterostructure, which is lower than those of RuO_2 (115 mV dec^{-1}), NiOOH (142 mV dec^{-1}) and
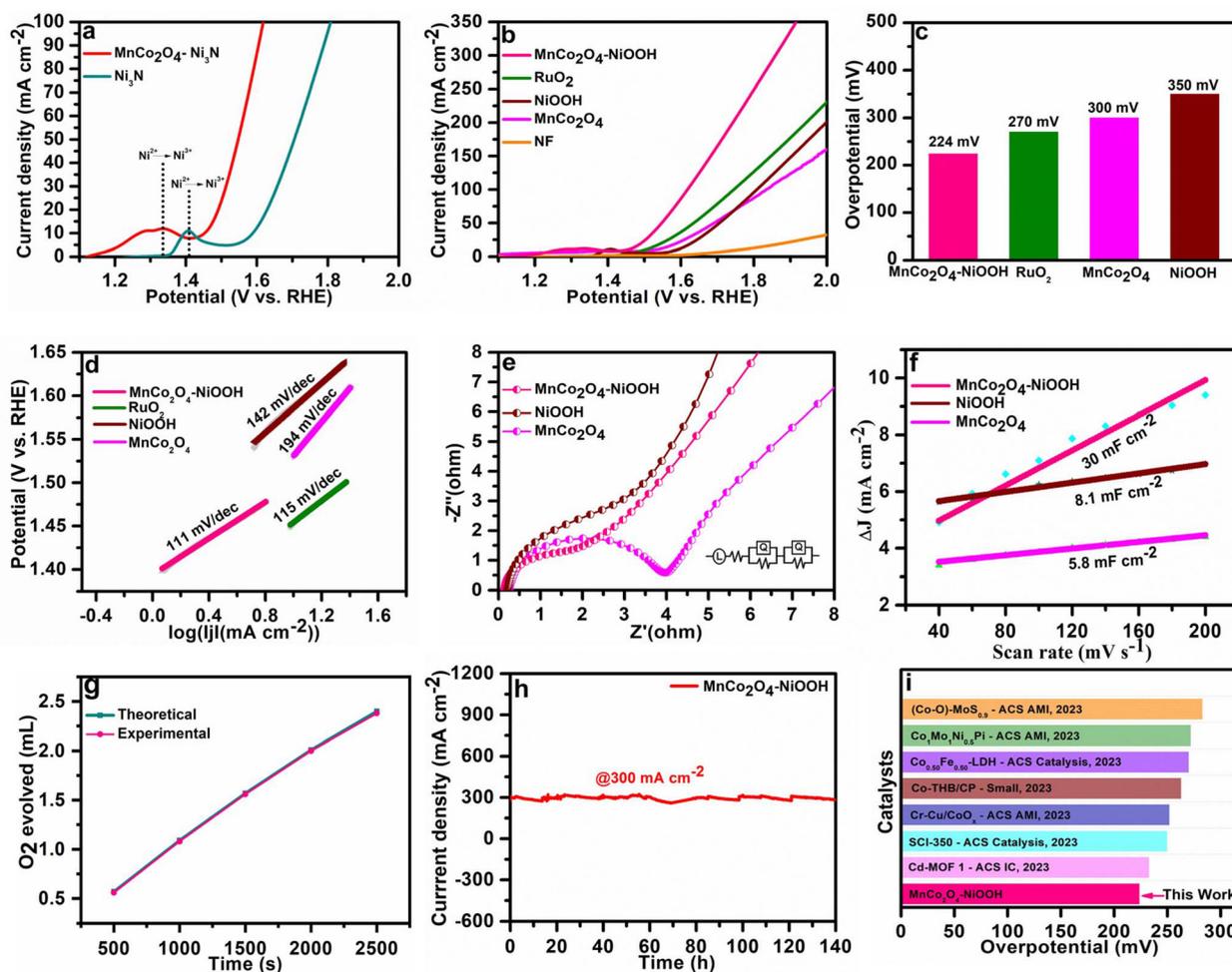
Fig. 4 (a) Polarization curve showing the position of the oxidation peak. (b) Polarization curve for the OER activity of $MnCo_2O_4$–NiOOH and other supporting catalysts. (c) Overpotential at 10 mA cm^{-2} of current density. (d) Tafel slope values of all the catalysts. (e) EIS Nyquist plots and (f) double layer capacitance of $MnCo_2O_4$–NiOOH, NiOOH and $MnCo_2O_4$. (g) Faradic efficiency of $MnCo_2O_4$–NiOOH. (h) Stability study using chronoamperometry. (i) Overpotential comparison with recently reported catalysts.

$MnCo_2O_4$ (194 mV dec^{-1}). The smaller Tafel slope value of the catalyst implies that the heterostructure likely exhibits quicker reaction kinetics than the separate phases.

Electrochemical impedance spectroscopy was used to assess the charge transfer resistance to estimate the interfacial interaction necessary for quicker electron transfer over the interface of electrode and electrolyte. The Nyquist plots of $MnCo_2O_4$–NiOOH, NiOOH and $MnCo_2O_4$ at 200 mV of overpotential are provided in Fig. 4e. The $MnCo_2O_4$–NiOOH heterostructure exhibited a lower R_{ct} value. This lower value of R_{ct} implies that there are a significant number of electrochemically active sites on the surface of the electrode, and that there is also a significant amount of interfacial charge transfer. These outcomes from the Nyquist plot indicate that there is a considerable increase in OER activity as well. We examined the electrochemical C_{dl} of the $MnCo_2O_4$–NiOOH catalyst to obtain an accurate evaluation of the OER activity that is inherently present in the reported catalyst. The C_{dl} was calculated using cyclic voltammetry scans performed between 0.01 to 0.1 V (V vs. Ag/AgCl) with varying scan rates of 20 to 200 mV s^{-1} (ESI S4.1 Fig. S4†). The obtained C_{dl} values for $MnCo_2O_4$–NiOOH, NiOOH, and $MnCo_2O_4$ are 30, 8.1, and 5.8 mF cm^{-2}, respectively (Fig. 4f). The significance of the electrochemical active surface area (ECSA) in the realm of electrocatalysis is underscored by various important factors. Gaining understanding of these concepts can offer valuable perspectives on the development and assessment of electrocatalysts. ECSA is a measure that accurately reflects the actual surface area of an electrode that is accessible for electrochemical processes. A higher ECSA value corresponds to an increased number of accessible sites for reactant molecules to adsorb and undergo the intended electrochemical transition. The pace at which these reactions occur is directly influenced by this factor, thereby impacting the overall efficiency and performance of the electrochemical system.

The electrochemically active surface area (ECSA) was computed from the C_{dl} values, and the obtained ECSA values for $MnCo_2O_4$–NiOOH, NiOOH, and $MnCo_2O_4$ were 75, 20.25, and 14.5 cm^2, respectively. A high ECSA value signifies that the catalytic surface contains a significant number of active sites. We also normalized the LSV curves of all the catalysts using ECSA, and the heterostructure is still highly active than that of the individual $MnCo_2O_4$ and NiOOH phases (ESI S4.2 Fig. S6†). By comparing the amount of oxygen (O_2) evolved experimentally with the theoretical amount of oxygen (O_2) evolved, we can estimate the faradic efficiency using the water–gas displacement method. Our catalyst has a faradic efficiency of 98.5% (Fig. 4g). The chronoamperometry technique was utilized to investigate the long-term durability of the $MnCo_2O_4$–NiOOH catalyst for the OER. As can be observed in Fig. 4h, a continuous durability test lasting 140 hours was conducted with chronoamperometry at a very high current density of 300 mA cm^{-2}. Based on the results of this experiment, the $MnCo_2O_4$–NiOOH catalyst is exceptionally stable even when subjected to harsh conditions. Comparing the activity of the majority of the reported $MnCo_2O_4$- and Ni_3N-based catalysts

(Fig. 4i), we observed that the present catalyst exhibits significantly low overpotential. The details of the catalyst documented here are provided in ESI S4.3 Table S1.†

To investigate the surface of the catalyst after a long-term durability test, we used the TEM and SEM techniques. The TEM image (Fig. 5a) shows the presence of $MnCo_2O_4$ nanowires wrapped by NiOOH sheets. HRTEM analysis (Fig. 5b–d) also confirms the presence of $MnCo_2O_4$ and NiOOH phases. The SEM images confirm the retention of the nano-urchin morphology (Fig. 5e–g). The elemental mapping of the catalyst after stability testing confirms the presence of Ni, Mn, Co, and O after the long-term durability tests (Fig. 5h–l). We also analysed the valence state of the elements present in the catalyst after the stability test. We did not find any change in the XPS spectra after the long-term durability test (ESI S4.4 Fig. S7†).

DFT calculations

DFT modelling was used to provide an understanding of the precise mechanism underlying the OER. A theoretical model was constructed, as illustrated in Fig. 6a and b, to more effectively depict the synergistic action in $MnCo_2O_4$–NiOOH. Fig. 6c shows the OER process in an alkaline medium, which comprises four intermediates: (i) OH* is adsorbed on the metal active site; (ii) O* is formed; (iii) OOH* is produced; (iv) O_2 is evolved; and the active site is left unoccupied, which is employed for more oxygen evolution. In the ESI (ESI) section S5, Tables S2–S5† contain a description of how the adsorption energy was calculated. The projected orbital density of state (DOS) plots for the d-orbitals are shown in Fig. 6d. The area under the curve embodies the number of occupied electronic states at each energy level. It was observed that $MnCo_2O_4$–NiOOH exhibits a considerably larger density of states at the Fermi level as compared to $MnCo_2O_4$ and NiOOH individually. This substantial increase in the density of states of the d-orbitals at the Fermi level after introducing NiOOH into $MnCo_2O_4$ leads to faster and more efficient charge transfer. Additionally, the significant active site in the process of catalyzing the OER was identified by computing the change in Gibbs free energy (ΔG) of each elementary step of the catalyst. Fig. 6e and f present the ΔG value (at U = 1.23 V and 0 V) of the catalyst. It was found that the ΔG value of the rate-limiting step (RLS) is lower in the case of $MnCo_2O_4$–Ni*OOH (1.03 V) as compared to those of Mn*Co_2O_4 (2.55 V), MnCo*$_2O_4$ (1.63 V), and Ni*OOH (1.23 V) (* signifies the catalyst site). The analysis revealed that the incorporation of NiOOH into the $MnCo_2O_4$ decreased the ΔG value of the RLS, and the rate of reaction increased.

Overall water splitting activity

Motivated by the favourable oxygen evolution reaction (OER) activity, the $MnCo_2O_4$–NiOOH composite was utilized as an anode, and Pt/C was used as the cathode, in order to evaluate the water splitting performance. Fig. 7a shows a schematic representation of the Pt/C‖$MnCo_2O_4$–NiOOH cell. We obtained a very low cell potential of 1.46 V to drive a current density of 10 mA cm^{-2}, which is superior to that of Pt/C‖RuO_2 (Fig. 7b).
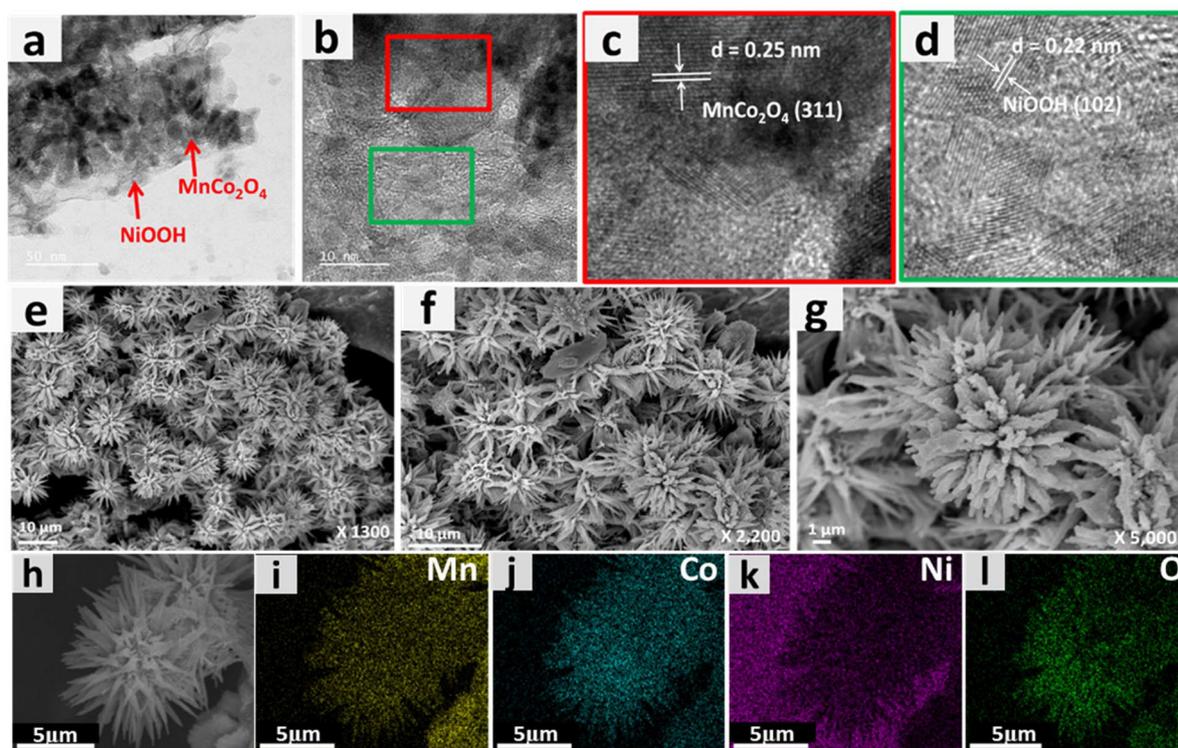
Fig. 5 (a) TEM image after the durability test. (b), (c) and (d) HRTEM images after the durability test confirming the presence of (c) $MnCo_2O_4$ and (d) NiOOH. (e–g) FESEM images of $MnCo_2O_4$–NiOOH after the durability test. (h–l) FESEM elemental mapping of the catalyst after the durability test.
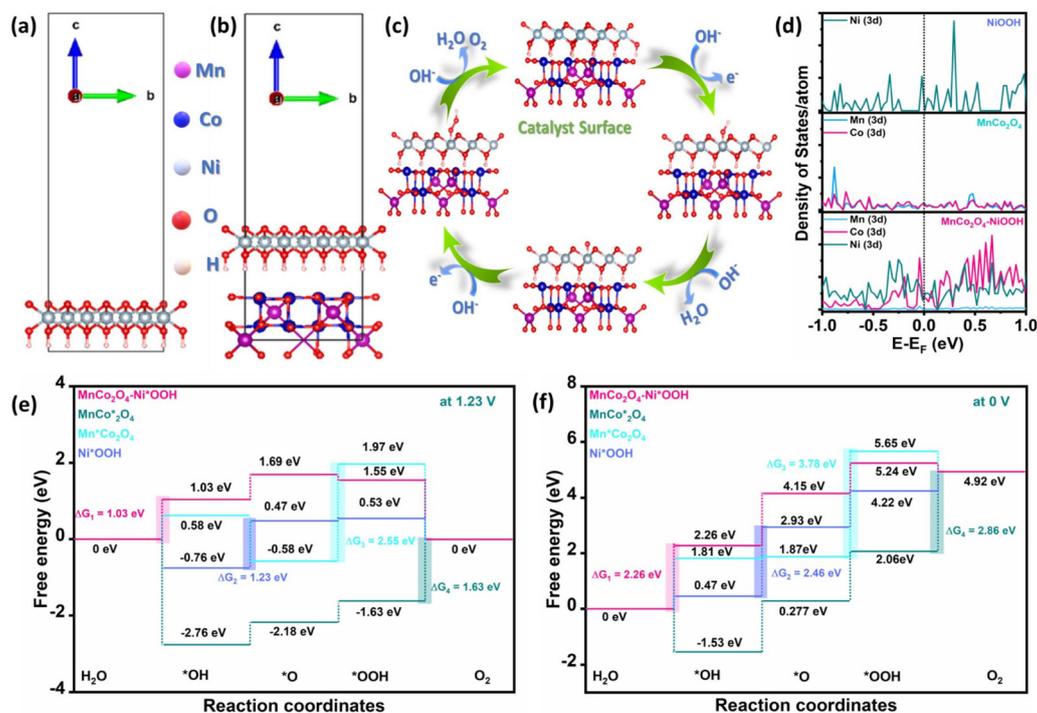
Fig. 6 Theoretical models of (a) $MnCo_2O_4$ and (b) $MnCo_2O_4$–NiOOH. (c) illustration of the mechnaism for the OER on the heterostructure(d) Projected orbital DOS plot. Gibbs free energy plot for the OER (e) at 1.23 V and (f) at 0 V for $MnCo_2O_4$, NiOOH, and $MnCo_2O_4$–NiOOH.
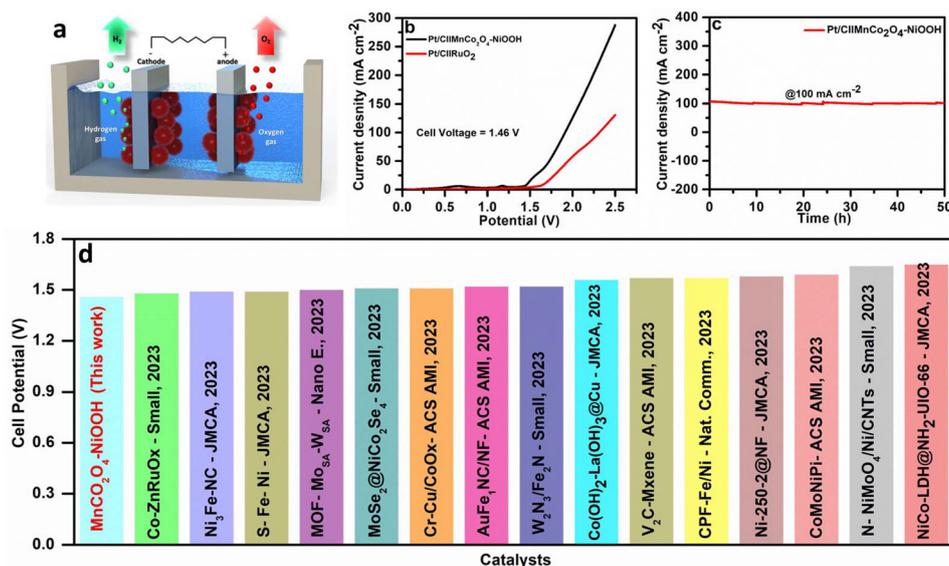
Fig. 7 (a) Schematic representation of the cell for overall water splitting. (b) LSV curve in two-electrode setup. (c) Durability test using chronoamperometry. (d) Comparison of cell potential with the cell potentials of recently reported catalysts.

The catalyst was also stable for 50 h, showing a continuous current density of 100 mA cm^{-2} (Fig. 7c). Additionally, this performance surpasses the majority of recently reported catalysts that do not contain noble metals (Fig. 7d). The details of the catalyst documented here are provided in ESI S6 Table S2.†

Conclusions

In summary, the heterostructure MnCo$_2$O$_4$–Ni$_3$N shows rapid phase transformation to form MnCo$_2$O$_4$–NiOOH. The rapid phase transformation was governed by the strong coupling effect between MnCo$_2$O$_4$ and Ni$_3$N, which results in electronic reallocation through the interface. The catalyst MnCo$_2$O$_4$–NiOOH exhibits an overpotential of 224 mV and is far superior to MnCo$_2$O$_4$ or NiOOH alone. The electronic reallocation was extensively examined using X-ray photoelectron spectroscopy (XPS), which revealed a shift towards higher binding energy for Ni and N and towards lower binding energy for Mn, Co, and O. The MnCo$_2$O$_4$–NiOOH heterostructure shows stability for up to 140 h at a high current density of 300 mA cm^{-2}. The DFT studies also revealed that the NiOOH formed over the MnCo$_2$O$_4$ nanowires is more active than that of NiOOH alone. Nanostructures with carefully engineered interfaces are a necessary step in developing cutting-edge methods for energy conversion.

Author contributions

V. B. and A. G. thought of the idea for this piece of work. A. G. and J. M. J. did the synthesis and performed the detailed characterization. A. A. and C. B. performed the theoretical calculations. J. S., V. P., R. K. and K. G. helped in the data analysis and representation. A. G. and V. B. wrote the manuscript. The final draft of the article has been reviewed and approved by all authors.

Conflicts of interest

There are no conflicts to declare.

References

1 D. C. R. Hans-Otto Pörtner, M. M. B. Tignor, E. Poloczanska, K. Mintenbeck, A. Alegría, M. Craig, S. Langsdorf, S. Löschke, V. Möller, A. Okem and B. Rama, Contribution to the Sixth Assessment Report of the Intergovernmental Panel on Climate Change, *Climate Change 2022: Impacts, Adaptation and Vulnerability*, 2022, p. 3005.
2 L. Li, P. Wang, Q. Shao and X. Huang, Metallic nanostructures with low dimensionality for electrochemical water splitting, *Chem. Soc. Rev.*, 2020, **49**(10), 3072–3106.
3 B. Zhang, Y. Zheng, T. Ma, C. Yang, Y. Peng, Z. Zhou, M. Zhou, S. Li, Y. Wang and C. Cheng, Designing MOF Nanoarchitectures for Electrochemical Water Splitting, *Adv. Mater.*, 2021, **33**(17), 2006042.
4 E. Enkhtuvshin, S. Yeo, H. Choi, K. M. Kim, B.-S. An, S. Biswas, Y. Lee, A. K. Nayak, J. U. Jang, K.-H. Na,

W.-Y. Choi, G. Ali, K. H. Chae, M. Akbar, K. Y. Chung, K. Yoo, Y.-C. Chung, T. H. Shin, H. Kim, C.-Y. Chung and H. Han, Surface Reconstruction of Ni–Fe Layered Double Hydroxide Inducing Chloride Ion Blocking Materials for Outstanding Overall Seawater Splitting, *Adv. Funct. Mater.*, 2023, **33**(22), 2214069.

5 H. Han, S. J. Kim, S. Y. Jung, D. Oh, A. K. Nayak, J. U. Jang, J. Bang, S. Yeo and T. H. Shin, Amorphous-Crystalline Interfaces on Hollow Nanocubes Derived from Ir-Doped Ni–Fe–Zn Prussian Blue Analog Enables High Capability of Alkaline/Acidic/Saline Water Oxidations, *Small*, 2023, 2303912.

6 R. R. Rao, I. E. L. Stephens and J. R. Durrant, Understanding What Controls the Rate of Electrochemical Oxygen Evolution, *Joule*, 2021, **5**(1), 16–18.

7 J. Wang, S.-J. Kim, J. Liu, Y. Gao, S. Choi, J. Han, H. Shin, S. Jo, J. Kim, F. Ciucci, H. Kim, Q. Li, W. Yang, X. Long, S. Yang, S.-P. Cho, K. H. Chae, M. G. Kim, H. Kim and J. Lim, Redirecting dynamic surface restructuring of a layered transition metal oxide catalyst for superior water oxidation, *Nat. Catal.*, 2021, **4**(3), 212–222.

8 C. Baeumer, J. Li, Q. Lu, A. Y.-L. Liang, L. Jin, H. P. Martins, T. Duchoň, M. Glöß, S. M. Gericke, M. A. Wohlgemuth, M. Giesen, E. E. Penn, R. Dittmann, F. Gunkel, R. Waser, M. Bajdich, S. Nemšák, J. T. Mefford and W. C. Chueh, Tuning electrochemically driven surface transformation in atomically flat LaNiO3 thin films for enhanced water electrolysis, *Nat. Mater.*, 2021, **20**(5), 674–682.

9 C. Lei, Q. Zheng, F. Cheng, Y. Hou, B. Yang, Z. Li, Z. Wen, L. Lei, G. Chai and X. Feng, High-Performance Metal-Free Nanosheets Array Electrocatalyst for Oxygen Evolution Reaction in Acid, *Adv. Funct. Mater.*, 2020, **30**(31), 2003000.

10 H. B. Tao, Y. Xu, X. Huang, J. Chen, L. Pei, J. Zhang, J. G. Chen and B. Liu, A General Method to Probe Oxygen Evolution Intermediates at Operating Conditions, *Joule*, 2019, **3**(6), 1498–1509.

11 Y. Liu, Y. Wang, S. Zhao and Z. Tang, Metal–Organic Framework-Based Nanomaterials for Electrocatalytic Oxygen Evolution, *Small Methods*, 2022, **6**(10), 2200773.

12 S. Zhao, Y. Yang and Z. Tang, Insight into Structural Evolution, Active Sites, and Stability of Heterogeneous Electrocatalysts, *Angew. Chem., Int. Ed.*, 2022, **61**(11), e202110186.

13 W. Cheng, X. Zhao, H. Su, F. Tang, W. Che, H. Zhang and Q. Liu, Lattice-strained metal–organic-framework arrays for bifunctional oxygen electrocatalysis, *Nat. Energy*, 2019, **4**(2), 115–122.

14 A. Joshi, P. Sood, A. Gaur, D. Rani, V. Madaan and M. Singh, Improved OER performance of an Anderson-supported cobalt coordination polymer by assembling with acetylene black, *J. Mater. Chem. A*, 2022, **10**(24), 12805–12810.

15 I. Yamada, H. Fujii, A. Takamatsu, H. Ikeno, K. Wada, H. Tsukasaki, S. Kawaguchi, S. Mori and S. Yagi, Bifunctional Oxygen Reaction Catalysis of Quadruple Manganese Perovskites, *Adv. Mater.*, 2017, **29**(4), 1603004.

16 Y. Zhou, S. Sun, C. Wei, Y. Sun, P. Xi, Z. Feng and Z. J. Xu, Significance of Engineering the Octahedral Units to Promote the Oxygen Evolution Reaction of Spinel Oxides, *Adv. Mater.*, 2019, **31**(41), 1902509.

17 A. K. Shah and M. Qureshi, In Situ Grown Cuboidal MnCo2O4/h Boron Nitride Heterojunction: A Noble Metal-Free Approach Based on Efficient Hole Extraction for Electrochemical Oxygen Evolution Reaction, *ACS Appl. Energy Mater.*, 2022, **5**(2), 1551–1559.

18 J. Y. C. Chen, J. T. Miller, J. B. Gerken and S. S. Stahl, Inverse spinel NiFeAlO4 as a highly active oxygen evolution electrocatalyst: promotion of activity by a redox-inert metal ion, *Energy Environ. Sci.*, 2014, **7**(4), 1382–1386.

19 H. Han, Y. Qiu, H. Zhang, T. Bi, Q. Yang, M. Liu, J. Zhou and X. Ji, Lattice-disorder layer generation from liquid processing at room temperature with boosted nanointerface exposure toward water splitting, *Sustainable Energy Fuels*, 2022, **6**(12), 3008–3013.

20 Y. Qiu, Z. Liu, Q. Yang, X. Zhang, J. Liu, M. Liu, T. Bi and X. Ji, Atmospheric-Temperature Chain Reaction towards Ultrathin Non-Crystal-Phase Construction for Highly Efficient Water Splitting, *Chem. – Eur. J.*, 2022, **28**(51), e202200683.

21 J. Luo, X. Wang, Y. Gu, D. Wang, S. Wang, W. Li, Y. Zhou and J. Zhang, Constructing hollow nanocages of Co3O4-CoMoO4 heterostructure for efficient electrocatalytic oxygen evolution reaction, *Appl. Surf. Sci.*, 2022, **606**, 154562.

22 Y. Pan, H. Ren, R. Chen, Y. Wu and D. Chu, Enhanced electrocatalytic oxygen evolution by manipulation of electron transfer through cobalt-phosphorous bridging, *Chem. Eng. J.*, 2020, **398**, 125660.

23 D. Gao, J. Zhang, T. Wang, W. Xiao, K. Tao, D. Xue and J. Ding, Metallic Ni3N nanosheets with exposed active surface sites for efficient hydrogen evolution, *J. Mater. Chem. A*, 2016, **4**(44), 17363–17369.

24 B. You, X. Liu, G. Hu, S. Gul, J. Yano, D.-e. Jiang and Y. Sun, Universal Surface Engineering of Transition Metals for Superior Electrocatalytic Hydrogen Evolution in Neutral Water, *J. Am. Chem. Soc.*, 2017, **139**(35), 12283–12290.

25 K. Xu, P. Chen, X. Li, Y. Tong, H. Ding, X. Wu, W. Chu, Z. Peng, C. Wu and Y. Xie, Metallic Nickel Nitride Nanosheets Realizing Enhanced Electrochemical Water Oxidation, *J. Am. Chem. Soc.*, 2015, **137**(12), 4119–4125.

26 Z. Liu, M. Zha, Q. Wang, G. Hu and L. Feng, Overall water-splitting reaction efficiently catalyzed by a novel bi-functional Ru/Ni3N–Ni electrode, *Chem. Commun.*, 2020, **56**(15), 2352–2355.

27 M. Wang, W. Ma, Z. Lv, D. Liu, K. Jian and J. Dang, Co-Doped Ni3N Nanosheets with Electron Redistribution as Bifunctional Electrocatalysts for Efficient Water Splitting, *J. Phys. Chem. Lett.*, 2021, **12**(6), 1581–1587.

28 A. Wu, Y. Xie, H. Ma, C. Tian, Y. Gu, H. Yan, X. Zhang, G. Yang and H. Fu, Integrating the active OER and HER components as the heterostructures for the efficient overall water splitting, *Nano Energy*, 2018, **44**, 353–363.

29 A. Gaur, J. M. John, V. Pundir, R. Kaur and V. Bagchi, Electronegativity-Induced Valence State Augmentation of Ni and Co through Electronic Redistribution between Co-Ni3N/CeF3 Interfaces for Oxygen Evolution Reaction, *ACS Appl. Energy Mater.*, 2023, **6**(3), 1763–1770.

30 C. Ray, S. C. Lee, B. Jin, A. Kundu, J. H. Park and S. Chan Jun, Conceptual design of three-dimensional CoN/Ni3N-coupled nanograsses integrated on N-doped carbon to serve as efficient and robust water splitting electrocatalysts, *J. Mater. Chem. A*, 2018, **6**(10), 4466–4476.

31 X. Gao, X. Liu, W. Zang, H. Dong, Y. Pang, Z. Kou, P. Wang, Z. Pan, S. Wei, S. Mu and J. Wang, Synergizing in-grown Ni3N/Ni heterostructured core and ultrathin Ni3N surface shell enables self-adaptive surface reconfiguration and efficient oxygen evolution reaction, *Nano Energy*, 2020, **78**, 105355.

32 M. Zhao, W. Yuan and C. M. Li, Controlled self-assembly of Ni foam supported poly (ethyleneimine)/reduced graphene oxide three-dimensional composite electrodes with remarkable synergistic effects for efficient oxygen evolution, *J. Mater. Chem. A*, 2017, **5**(3), 1201–1210.

33 F. Wang, G. Chen, X. Liu, F. Chen, H. Wan, L. Ni, N. Zhang, R. Ma and G. Qiu, Advanced Electrocatalytic Performance of Ni-Based Materials for Oxygen Evolution Reaction, *ACS Sustainable Chem. Eng.*, 2019, **7**(1), 341–349.

34 Q. Zhou, T.-T. Li, F. Guo and Y.-Q. Zheng, Construction of Hierarchically Structured CuO@CoP Anode for Efficient Oxygen Evolution Reaction, *ACS Sustainable Chem. Eng.*, 2018, **6**(9), 11303–11312.

35 J. Luo, X. H. Wang, L. Shen, H. C. Fu, X. H. Chen, L. L. Wu, Q. Zhang, H. Q. Luo and N. B. Li, Corrosion-Engineered Mo-Containing FeCo-(oxy)hydroxide Electrocatalysts for Superior Oxygen Evolution Reaction, *ACS Sustainable Chem. Eng.*, 2021, **9**(36), 12233–12241.

36 S. Sirisomboonchai, S. Li, A. Yoshida, X. Li, C. Samart, A. Abudula and G. Guan, Fabrication of NiO Microflake@NiFe-LDH Nanosheet Heterostructure Electrocatalysts for Oxygen Evolution Reaction, *ACS Sustainable Chem. Eng.*, 2019, **7**(2), 2327–2334.

37 M. Zhao, H. Li, W. Yuan and C. M. Li, Tannic acid-mediated in situ controlled assembly of NiFe alloy nanoparticles on pristine graphene as a superior oxygen evolution catalyst, *ACS Appl. Energy Mater.*, 2020, **3**(4), 3966–3977.

38 J. Bai, J. Mei, T. Liao, Q. Sun, Z.-G. Chen and Z. Sun, Molybdenum-Promoted Surface Reconstruction in Polymorphic Cobalt for Initiating Rapid Oxygen Evolution, *Adv. Energy Mater.*, 2022, **12**(5), 2103247.

39 C. Wang, P. Zhai, M. Xia, W. Liu, J. Gao, L. Sun and J. Hou, Identification of the Origin for Reconstructed Active Sites on Oxyhydroxide for Oxygen Evolution Reaction, *Adv. Mater.*, 2023, **35**(6), 2209307.

40 J. Zhang, W. He, H. B. Aiyappa, T. Quast, S. Dieckhöfer, D. Öhl, J. R. C. Junqueira, Y.-T. Chen, J. Masa and W. Schuhmann, Hollow CeO$_2$@Co2N Nanosheets Derived from Co-ZIF-L for Boosting the Oxygen Evolution Reaction, *Adv. Mater. Interfaces*, 2021, **8**(9), 2100041.

41 J. Ge, W. Zhang, J. Tu, T. Xia, S. Chen and G. Xie, Suppressed Jahn–Teller Distortion in MnCo2O4@Ni2P Heterostructures to Promote the Overall Water Splitting, *Small*, 2020, **16**(34), 2001856.

42 J. Sun, J. Lu, C. Huang, Q. Wu, L. Xia, Q. Xu and W. Yao, Modification of Ni3N with a Cobalt-Doped Carbon Shell for High-Performance Hydrogen Evolution in Alkaline Media, *ACS Sustainable Chem. Eng.*, 2021, **9**(5), 1994–2002.

43 G. S. Shanker and S. Ogale, Faceted Colloidal Metallic Ni3N Nanocrystals: Size-Controlled Solution-Phase Synthesis and Electrochemical Overall Water Splitting, *ACS Appl. Energy Mater.*, 2021, **4**(3), 2165–2173.

44 Y. Yang, Q. Dai, Q. Shi, Y. Liu, T. T. Isimjan and X. Yang, Electronic Modulation of Pt Nanoparticles on Ni3N–Mo2C by Support-Induced Strategy for Accelerating Hydrogen Oxidation and Evolution, *J. Phys. Chem. Lett.*, 2022, **13**(9), 2107–2116.

45 M. Yang, M. Zhao, J. Yuan, J. Luo, J. Zhang, Z. Lu, D. Chen, X. Fu, L. Wang and C. Liu, Oxygen Vacancies and Interface Engineering on Amorphous/Crystalline CrOx-Ni3N Heterostructures toward High-Durability and Kinetically Accelerated Water Splitting, *Small*, 2022, **18**(14), 2106554.

46 Y. Chen, J. Yu, J. Jia, F. Liu, Y. Zhang, G. Xiong, R. Zhang, R. Yang, D. Sun, H. Liu and W. Zhou, Metallic Ni3Mo3N Porous Microrods with Abundant Catalytic Sites as Efficient Electrocatalyst for Large Current Density and Superstability of Hydrogen Evolution Reaction and Water Splitting, *Appl. Catal., B*, 2020, **272**, 118956.

47 L. Qi, Z. Zheng, C. Xing, Z. Wang, X. Luan, Y. Xue, F. He and Y. Li, 1D Nanowire Heterojunction Electrocatalysts of MnCo2O4/GDY for Efficient Overall Water Splitting, *Adv. Funct. Mater.*, 2022, **32**(11), 2107179.

48 K. Zeng, W. Li, Y. Zhou, Z. Sun, C. Lu, J. Yan, J.-H. Choi and R. Yang, Multilayer hollow MnCo2O4 microsphere with oxygen vacancies as efficient electrocatalyst for oxygen evolution reaction, *Chem. Eng. J.*, 2021, **421**, 127831.

49 T.-H. Ko, K. Devarayan, M.-K. Seo, H.-Y. Kim and B.-S. Kim, Facile Synthesis of Core/Shell-like NiCo2O4-Decorated MWCNTs and its Excellent Electrocatalytic Activity for Methanol Oxidation, *Sci. Rep.*, 2016, **6**(1), 20313.

50 J. F. Marco, J. R. Gancedo, M. Gracia, J. L. Gautier, E. Ríos and F. J. Berry, Characterization of the Nickel Cobaltite, NiCo2O4, Prepared by Several Methods: An XRD, XANES, EXAFS, and XPS Study, *J. Solid State Chem.*, 2000, **153**(1), 74–81.

51 Y. Mo, Q. Ru, X. Song, S. Hu, L. Guo and X. Chen, 3-dimensional porous NiCo2O4 nanocomposite as a high-rate capacity anode for lithium-ion batteries, *Electrochim. Acta*, 2015, **176**, 575–585.

52 R. Andaveh, G. Barati Darband and M. Maleki, Sabour Rouhaghdam, A., Superaerophobic/superhydrophilic surfaces as advanced electrocatalysts for the hydrogen evolution reaction: a comprehensive review, *J. Mater. Chem. A*, 2022, **10**(10), 5147–5173.

53 Q. Hu, G. Li, X. Liu, B. Zhu, X. Chai, Q. Zhang, J. Liu and C. He, Superhydrophilic Phytic-Acid-Doped Conductive Hydrogels as Metal-Free and Binder-Free Electrocatalysts for Efficient Water Oxidation, *Angew. Chem., Int. Ed.*, 2019, **58**(13), 4318–4322.

54 A. Gaur, Krishankant, V. Pundir, A. Singh, T. Maruyama, C. Bera and V. Bagchi, Intense nano-interfacial interactivity stimulates the OER in a MOF-derived superhydrophilic CuO–NiO heterostructure, *Sustainable Energy Fuels*, 2021, **5**(21), 5505–5512.